Effect of laser wavelength on the thermoelectric properties of $Bi_{1.6}Pb_{0.4}Sr_2Co_2O_8$ textured ceramics processed by LFZ

P. Amirkhizi [a,*], M.A. Madre [b], O.J. Dura [c], M.A. Torres [b], A. Sotelo [b], A. Kovalevsky [a], Sh. Rasekh [a]

[a] Department of Materials and Ceramic Engineering, CICECO-Aveiro Institute of Materials, University of Aveiro, 3810-193, Aveiro, Portugal
[b] INMA (CSIC-Universidad de Zaragoza), Mª de Luna 3, 50018, Zaragoza, Spain
[c] Applied Physics Department, University of Castilla-La Mancha, 13071, Ciudad Real, Spain

ARTICLE INFO

ABSTRACT

$Bi_{1.6}Pb_{0.4}Sr_2Co_2O_8$ samples have been textured by the Laser Floating Zone (LFZ) process using Nd:YAG, and CO_2 laser radiation. Using different wavelengths resulted in significant structural and microstructural modifications. Powder XRD patterns showed that the thermoelectric phase is the major one in both cases. Microstructural studies revealed that all samples presented the same phases but with much lower content of secondary ones in those processed with the CO_2 laser. Electrical resistivity showed different behavior for the two types of samples, being in general, lower for the CO_2 grown rods. Seebeck coefficient is lower for the CO_2 grown samples up to 300 °C, and higher in the high-temperature range, reaching 240 μV/K at 650 °C, which is one of the highest values obtained so far in these compounds. Moreover, thermal conductivity at 600 °C for these samples (0.93 W/K m) is among the lowest reported in the literature. As a consequence, ZT values at 600 °C reached 0.42 in CO_2 textured materials, about two times higher than the obtained in Nd:YAG ones. This value is among the highest reported so far in the literature, and is comparable to the performance attained for the same composition containing nanoparticles addition. All these properties, combined with the fact that the processed materials can be directly integrated into thermoelectric modules, render them highly attractive for industrial production.

1. Introduction

Nowadays, thermoelectric heat harvesting is regarded as one of the most important technologies for co-generation by converting waste heat into useful electric power [1–3]. As it is well known, most of the processes using fossil fuels dissipate around 60 % of the initial energy into wasted heat. This is a huge problem, not only from the economic and resource consumption points of view, but also for the large amount of greenhouse gases emitted. Consequently, the use of these thermoelectric devices can help to reduce fossil fuel consumption by increasing the energy conversion efficiency, and thus helping to fight the global warming by decreasing the release of greenhouse gases. For these applications, it is necessary, in a first stage, producing materials with high thermoelectric performances, which are evaluated through the dimensionless Figure of Merit, ZT. It is defined as: $ZT = TS^2/\rho\kappa$, where T is the absolute temperature, S, the Seebeck coefficient, ρ, the electric resistivity, and κ, the thermal conductivity [4]. Moreover, it should be noted that thermoelectric modules are typically built using two different types of thermoelectric materials, called legs, which are n-, and p-type conductors. Due to this structure, the power extracted from the thermoelectric modules is associated not only to the ZT values of each type of leg forming the thermocouples [5], but also to the thermal and electrical resistance of their contacts [6].

Today, the most common commercial modules use intermetallic compounds as legs due to their high thermoelectric performances [7,8]. On the other hand, they are known for their tendency to oxidize at relatively high temperatures under air [9], their low abundance in the Earth's crust, and high costs [10–12]. The discovery of promising thermoelectric properties in a ceramic oxide, Na_xCoO_2 [13], was one of the steps towards the development of stable materials and structures which can potentially avoid these inconveniences [14]. Moreover, it led to an increased interest in these oxides, and other compounds were found to have relatively good thermoelectric properties, such as $Bi_2Sr_2Co_2O_8$ [15], $Ca_3Co_4O_9$ [16], or $CaMnO_3$ [17] to be used in thermoelectric modules. However, the oxide compounds still have relatively low ZT values, and many efforts are focused on enhancing their

properties through different approaches such as doping [18], entropy engineering [19], or grain alignment through hot uniaxial pressing [20], spark plasma sintering [21], or laser floating zone melting (LFZ) [22]. The grain alignment takes advantage of the crystal anisotropy of the cobalt oxide-based compounds, allowing orienting their ab-plane (which is also the conducting one) along the electrical conduction direction [23].

The melt grown techniques to produce highly textured materials have been applied for many years to different ceramic materials, as the image furnaces typically used to produce single crystals [24], or the laser melting zone [22]. The main differences between both techniques are related to the molten zone volume, much lower for the laser technique, together with the larger thermal gradient achieved in the solidification interface [25,26], allowing higher growth rates. On the other hand, the laser source in the LFZ process may play an important role in the growth conditions, especially in the thermal radial gradient which drastically influences the grain orientation as reported in similar systems [27]. In this work, different wavelength lasers, Nd:YAG ($\lambda = 1064$ nm), and CO_2 ($\lambda = 10.6$ μm) were used in the Laser Floating Zone (LFZ) method for melt-growing $Bi_{1.6}Pb_{0.4}Sr_2Co_2O_8$ thermoelectric ceramics. The difference between the two types of laser lies in the different penetration of the radiation, much greater in the case of the Nd-YAG laser, which should produce a molten zone with a more homogeneous temperature distribution. However, other factors, as the radial thermal gradient may vary depending on the laser wavelength. Consequently, the effect of the different lasers on the structure and microstructure of these samples has been studied and related to the thermoelectric performances of these bulk textured materials.

2. Experimental

The $Bi_{1.6}Pb_{0.4}Sr_2Co_2O_8$ precursors were prepared using appropriate amounts of Bi_2O_3 (98 + %, Panreac), PbO (99.9 %, Aldrich), $SrCO_3$ (≥98%, Aldrich), and Co_3O_4 (99.5 %, Aldrich) powders. They were weighed in the appropriate proportions, mixed and ball milled at 300 rpm for 30 min in water media. After drying the suspension, the resulting powder was calcined in two steps: 750 °C for 12 h, and 800 °C for 12 h, with an intermediate manual milling. The objective of this process was mainly to decompose alkaline earth carbonates to avoid this process during the LFZ growth. Otherwise, it would lead to CO_2 bubbles formation in the molten zone, producing turbulences in the melt that can be reflected in grain misalignment [28], and various perturbations in the growth, leading to porosity and other undesirable defects. These powders were cold isostatically pressed in the shape of cylinders (~100 mm length and 2–3 mm Ø) under 250 MPa, and further used as feed in a LFZ system previously described [27]. All samples were grown in the same conditions, 30 mm/h and relative rotation between feed and seed of 18 rpm. For the sake of comparison, some samples were textured using Nd: YAG laser radiation, while for others CO_2 laser radiation was used. After the LFZ processing of samples, the rods with very regular dimensions (~2 mm Ø) were produced. On the other hand, these melt-solidified materials present a large number and amount of secondary phases due to their incongruent melting [29–31] Consequently, they were further annealed at 800 °C for 24 h to reduce the amount of secondary phases and maximize the thermoelectric phase content. Afterwards, they were cut in the adequate dimensions for further characterization.

The identification of phases in all samples has been performed using powder XRD diffraction (Rigaku Ru300) between 10 and 80°. Microstructural studies were performed, with backscattered electrons, on longitudinal polished sections of all samples in a FESEM microscope (Zeiss Merlin) equipped with an energy dispersive spectrometer (EDS) to evaluate the elemental composition. Simultaneous determination of Seebeck coefficient and electrical resistivity was performed in a LSR-3 system (Linseis GmbH) in steady state mode between 50 and 650 °C. Thermal conductivity (κ) was calculated using the well-known expression $\kappa = \alpha\, C_p\, d$, where α is thermal diffusivity, C_p the specific heat, and

d the sample density. The α parameter has been measured in a laser-flash system (Linseis LFA 1000) between 50 and 650 °C, along the same direction used for electrical characterization, while C_p has been determined through Dulong-Petit law. Finally, using both the electrical and thermal data, the temperature dependence of ZT was calculated for both types of samples, and compared to those presented in the literature for this type of compounds.

3. Results and discussion

Fig. 1 displays the powder XRD patterns of both types of samples. As it can be observed in the plot, the highest peaks correspond to the thermoelectric phase (indicated by their diffraction planes) indexed as P2/m group, in agreement with previously published data [32,33]. Moreover, the (*00l*) peaks are the most intense ones, indicating a good grain alignment with their ab-planes parallel to the sample holder surface. This effect is due to the large surface/thickness ratio of the thermoelectric grains, reflected in their preferential orientation during the powdered samples preparation for this analysis. This fact is very common in these type of compounds, associated to their anisotropic growth, leading to plate-like grains with large dimensions along the ab planes. On the other hand, weak diffraction peaks (shown by *) are associated to the $(Bi,Pb)_3SrO_x$ secondary phase with $R\overline{3}mH'$ space group [34], which is present in minor amount.

Fig. 2 presents representative SEM micrographs performed on longitudinal polished surfaces of all samples. These images show that all samples present a laminar orientation along the growth direction (indicated by the arrow), and a very low amount of porosity. Moreover, they are composed by three contrasts (identified by numbers), which have been associated to different phases by EDS analysis. These are the major thermoelectric phase (grey contrast, #1), Bi–Pb–Sr–O solid solution (light grey, #2), and Sr–Co–O solid solution (dark grey, #3). These phases appear due to the incongruent melting of this compound, and the presence of the thermoelectric phase has been produced by their recombination promoted by the thermal post-treatment. These observed phases agree well with the XRD data, even if phase #3 has not been
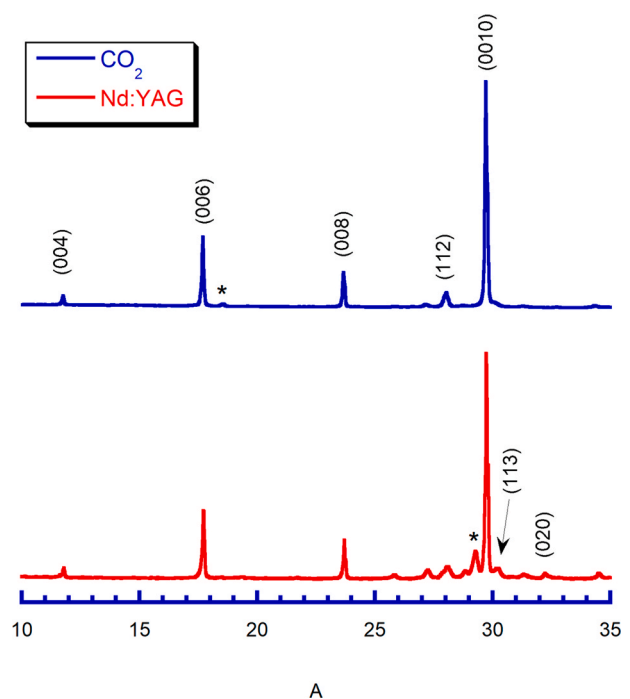

Fig. 1. Powder XRD patterns of both types of samples. Diffraction peaks of thermoelectric phase are identified by their planes. * shows the peaks corresponding to the $(Bi,Pb)_3SrO_x$ secondary phase.
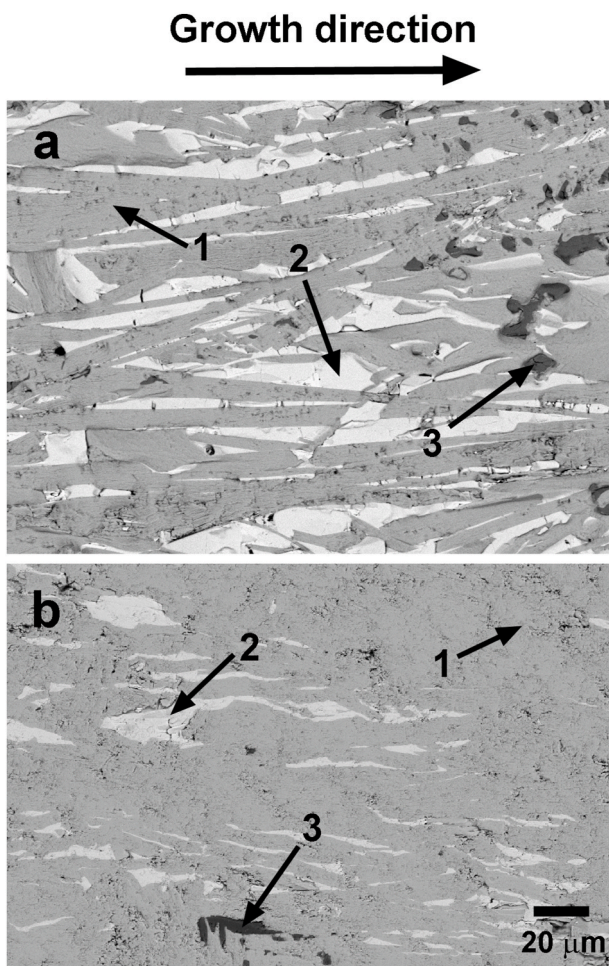
Growth direction

Fig. 2. Representative SEM micrographs of longitudinal polished sections of samples textured using a) Nd:YAG; and b) CO_2 laser radiation. The numbers show the different phases: #1 thermoelectric one; #2 Bi–Pb–Sr–O solid solution; and #3 Sr–Co–O solid solution.

detected, probably due to its low amount, and phase #2 is detected as minor one due to the overlapping of its main peaks with those of the thermoelectric phase. The differences between both types of samples are the lower amount of secondary phases, and the better grain orientation in samples grown using CO_2 laser radiation. These facts are due to the different penetration of radiation into the melt, as previously demonstrated [35]. As it has been shown, Nd:YAG is more penetrating and leads to a more homogeneous heating of the melt, while CO_2 heats more the rod surface. However, the solidification is more homogeneous in the second case, as it starts on the outer side of the rod, which is cooled by the surrounding atmosphere. This produces a large radial thermal gradient which leads to a separation of the secondary phases, as in the external part high melting point phases precipitate (in this case Sr–Co–O), while in the inner part, Bi(Pb)-rich phases appear. Furthermore, this large radial thermal gradient results in lower grain orientation, as previously reported for similar materials [36]. This effect is much less pronounced when CO_2 radiation is used, as the external part reaches higher temperatures than the internal one, and the phases are more homogeneously distributed. As a consequence, annealing significantly reduces the amount and sizes of secondary phases.

Fig. 3 illustrates the temperature dependence of the electrical resistivity for both types of samples. As it can be seen in the plot, samples grown with Nd:YAG laser radiation present semiconducting-like behavior ($d\rho/dT < 0$) from room temperature to around 450 °C and metallic-like one ($d\rho/dT > 0$) at higher temperatures. On the other hand,
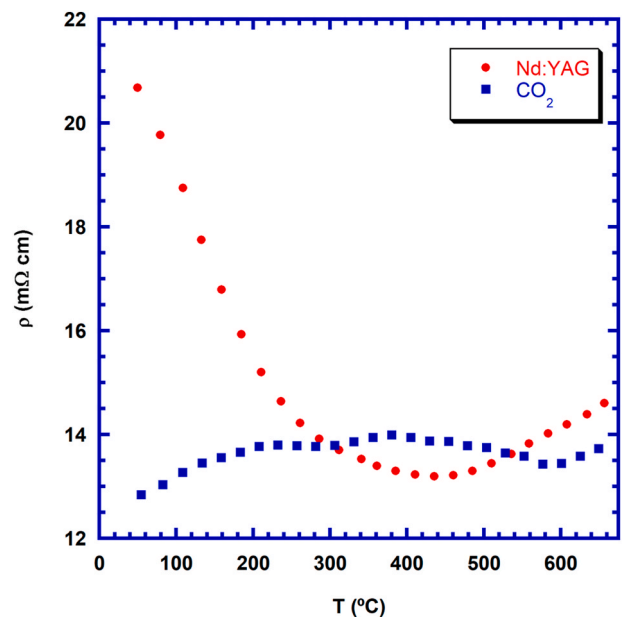

Fig. 3. Temperature dependence of electrical resistivity of samples as a function of the laser radiation.

CO_2 grown samples present metallic-like tendency in the whole measured temperature range. Previous works suggested that this alteration in the conductivity mechanism can be promoted by the changes in the average cobalt cation oxidation state [37], as well as microstructural and phase evolution [19]. Such a transition, also noted at significantly lower temperatures (50–150 K), was linked to strong electron correlations and Anderson localization [35] and single Anderson localization [38]. The behaviour of the Nd:YAG-grown sample, showing pronounced conductivity changes, is likely related to the lower phase purity as compared to CO_2 grown samples, which exhibit a metallic-type behaviour over the whole studied temperature range. Similar results were obtained in the work [19], where the non-annealed $Bi_2Sr_2Co_2O_y$ sample showed a pronounced semiconductor-metallic-type transition, while the samples of the same nominal composition after annealing and containing a lesser amount of impurities, displayed a weak temperature dependence of the electrical resistivity. Secondary phase segregation promotes a deviation of the composition of the major thermoelectric phase from nominal, accompanied by the formation of various defects (e.g., Bi vacancies), with different potential effects on the average cobalt oxidation state and charge carrier transport mechanism. The CO_2 grown samples display, in general, lower electrical resistivity values than those grown with the Nd:YAG laser. These facts can also be explained by the lower amount of secondary phases and the better grain orientation obtained by growing with the CO_2 laser due to the lower radial thermal gradients previously discussed in the SEM-EDS section. The minimum values at 650 °C have been measured in CO_2 grown samples (13.8 mΩ cm), which are lower than those reported in textured materials through hot-uniaxial-pressing (40 mΩ cm) [39], sintered (15–58 mΩ cm) [40–43] or processed through SPS (18 mΩ cm) [44]. Furthermore, they are quite close to the measured in single crystals (10 mΩ cm at 600 °C) [45].

The evolution of Seebeck coefficient with temperature for the samples grown by each laser type is shown in Fig. 4. At a first sight, it is clear that S is positive in the whole measured temperature range, confirming that they are p-type, and their conduction mechanism involves holes as the majority charge carriers. At room temperature, Nd:YAG grown samples display higher S than the CO_2 ones, in agreement with their higher electrical resistivity. Moreover, S is increased with temperature in all cases, with a higher slope for the CO_2 grown samples, producing a crossover at around 300 °C. These differences can be associated to a
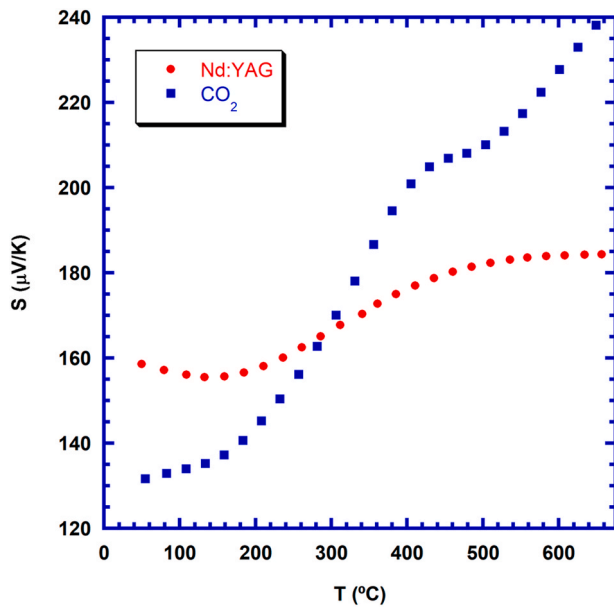
Fig. 4. Temperature dependence of Seebeck coefficient of samples as a function of the laser radiation.

Fig. 5. Temperature dependence of Power Factor of samples as a function of the laser radiation.

higher amount of thermoelectric phase in these samples. The highest S at 650 °C has been measured in CO_2 grown samples (~240 µV/K), which is much higher than the best reported for hot-pressed materials (150 µV/K) [39], single crystals (160 µV/K) [45], SPS processed (165 µV/K) [44], or sintered materials (150–210 µV/K) [41–43,46]. These very high S values obtained in these samples can be explained by the high amount of oxygen vacancies formed in the material during the laser melt-solidification process, as previously reported [47]. Despite the tendency to fill those vacancies during the annealing process under air, the oxygen diffusion through the bulk material is very limited due to its large density, leading to unusually high S values. Furthermore, the higher S values at room temperature for the Nd:YAG samples can be explained by the fact that they have larger amount of secondary phases, which would need larger amount of oxygen to produce the thermoelectric phase than those grown with the CO_2 laser. As a consequence, Nd:YAG samples have a higher amount of oxygen vacancies, reflected in lower charge carrier concentration, leading to higher S and ρ, than the measured in CO_2 grown ones.

Using the electrical resistivity and Seebeck coefficient values, power factor (PF=S^2/ρ) has been calculated and displayed in Fig. 5 in order to compare the electrical performances of samples. PF is higher in the whole measured temperature range for samples grown using CO_2 laser radiation, reaching 0.47 mW/K^2m, which is about 2 times higher than the obtained for Nd:YAG grown ones. Moreover, this value is much higher than those reported for hot-pressed materials (0.06 mW/K^2m) [39], SPS processed (0.06 mW/K^2m) [44], sintered bodies (0.14–0.25 mW/K^2m) [41–43,46], or single crystals (0.26 mW/K^2m) [45].

Fig. 6 presents the thermal conductivity evolution with temperature as a function of the laser radiation. As it can be observed in the plot, the thermal conductivity decreases with temperature, following the typical behavior previously reported [48,49]. Moreover, despite the higher thermal conductivity of samples textured using CO_2 radiation at low temperature, its decrease is more pronounced, producing a crossover at about 450 °C. The minimum values at 600 °C obtained in these samples (0.93 W/K m) are around 15 % lower than the obtained in samples grown with Nd:YAG radiation, likely due to a lesser amount of micron-scale secondary phases with a simpler crystalline structure and weaker phonon scattering ability. Moreover, it is among the best reported values for this type of materials (0.6–2.1 W/K m) [29,39,41,44, 48,49]. These low values of κ cannot be explained only through
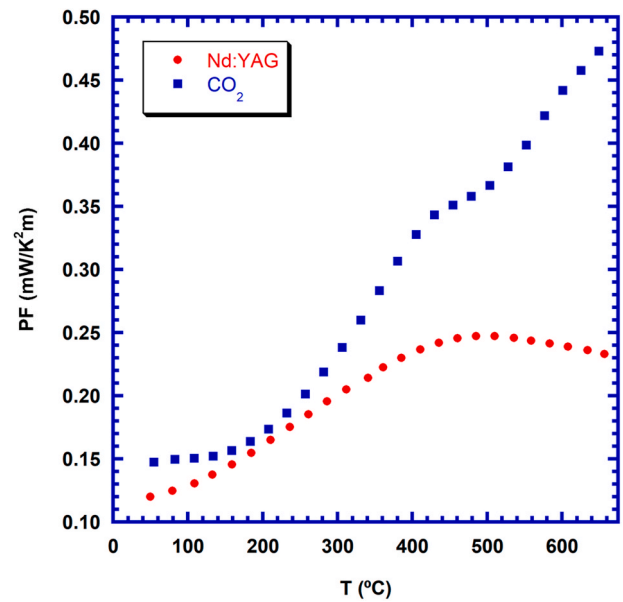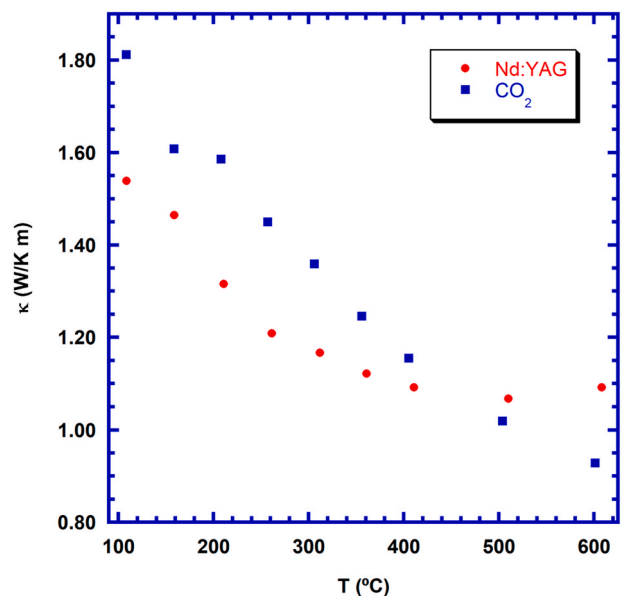

Fig. 6. Temperature dependence of thermal conductivity of samples as a function of the laser radiation.

phonon-phonon interactions and Pb doping, as there are other mechanisms that may affect it, such as the misfit factor between the subcells that form the crystal, as previously reported [48].

The ZT variation with temperature for all samples is shown in Fig. 7. As it can be seen in the plot, at low temperatures both samples display the same values up to around 300 °C. At higher temperatures, CO_2 grown samples display larger ZT values than Nd:YAG ones. The highest value at 600 °C (0.42) is more than two times higher than the obtained in Nd:YAG samples (0.19). Furthermore, it is one of the best reported for this material (0.11–0.41) [29,39,41,44,48,49], and relatively close to those obtained by addition of nanoparticles to the pristine material (0.48) [49]. Therefore, these results confirm that the thermoelectric properties of these materials can be enhanced by combining cationic substitution and texturing through the LFZ technique using CO_2 laser radiation. An additional advantage of this process is that the samples are
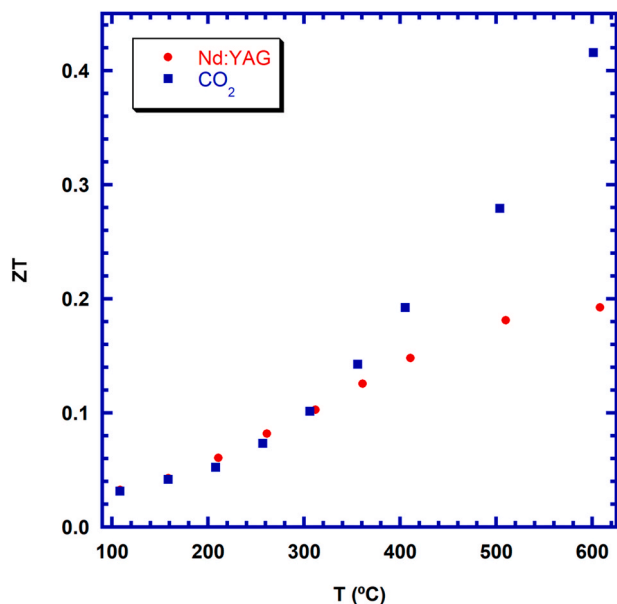
Fig. 7. Temperature dependence of ZT of samples as a function of the laser radiation.

prepared in form of long cylinders, with homogeneous diameter, which can be easily cut in the adequate length to directly assemble them into thermoelectric modules, avoiding long and expensive machining processes.

4. Conclusions

In this work, $Bi_{1.6}Pb_{0.4}Sr_2Co_2O_8$ samples have been prepared through the classical solid state method, and textured using the LFZ process using two different types of lasers, Nd:YAG, and CO_2. The characteristic wavelength of each laser produces different solidification front profiles, in agreement with previously reported data. Powder XRD characterization showed that the thermoelectric phase is the major one in both cases, with nearly no secondary phases. Microstructural studies revealed that all samples present two minor secondary phases besides the thermoelectric one. The use of CO_2 laser radiation drastically decreased the amount of secondary phases, when compared to those textured with the Nd:YAG one, and increased grain alignment. As a consequence, electrical resistivity was decreased, reaching 13.8 mΩ cm, and Seebeck coefficient increased up to 240 μV/K at 650 °C for the CO_2 grown rods. Moreover, thermal conductivity at 600 °C (0.93 W/K m) is also lower than the measured in Nd:YAG textured ones (1.09 W/K m). As a consequence, ZT values at 600 °C reached 0.42 in CO_2 textured materials, about two times higher than the obtained in Nd:YAG ones. All these characteristics, together with the possibility to avoid long and expensive machining processes to obtain thermoelectric legs for their integration in thermoelectric modules for power generation, make the LFZ process very attractive for industrial production of these materials.

Declaration of competing interest

The authors declare that they have no known competing financial interests or personal relationships that could have appeared to influence the work reported in this paper.

Acknowledgements

References

[1] L. Catalan, P. Alegria, M. Araiz, D. Astrain, Field test of a geothermal thermoelectric generator without moving parts on the Hot Dry Rock field of Timanfaya National Park, Appl. Therm. Eng. 222 (2023) 119843.
[2] D. Champier, Thermoelectric generators: a review of applications, Energy Conv. Manag. 140 (2017) 167–181.
[3] A.E. Risseh, H.P. Nee, O. Erlandsson, K. Brinkfeldt, A. Contet, F.F. Lng, G. Gaiser, A. Saramat, A. Saramat, T. Skare, S. Nee, J. Dellrud, Design of a thermoelectric generator for waste heat recovery application on a drivable heavy duty vehicle, SAE Int. J. Commer. Veh. 10 (2017) 26–44.
[4] D. M. Rowe, in: D. M. Rowe (Ed.), Thermoelectrics Handbook: Macro to Nano, CRC Press, Boca Raton, FL (USA), 2006..
[5] G. Min, D. M. Rowe, in: D. M. Rowe (Ed.), CRC Handbook of Thermoelectrics, CRC Press, London, 1995..
[6] D.M. Rowe, G. Min, Evaluation of thermoelectric modules for power generation, J. Power Sources 73 (1998) 193–198.
[7] J.A. Santamaria, J. Alkorta, J.G. Sevillano, Microcompression tests of single-crystalline and ultrafine grain Bi_2Te_3 thermoelectric material, J. Mater. Res. 30 (2015) 2593–2604.
[8] H. Wang, J. Hwang, M.L. Snedaker, I.-H. Kim, C. Kang, J. Kim, G.D. Stucky, J. Bowers, W. Kim, High thermoelectric performance of a heterogeneous PbTe nanocomposite, Chem. Mater. 27 (2015) 944–949.
[9] M.H. Elsheikh, D.A. Shnawah, M.F.M. Sabri, S.B.M. Said, M.H. Hassan, M.B. A. Bashir, M. Mohamad, A review on thermoelectric renewable energy: principle parameters that affect their performance, Renew. Sustain. Energy Rev. 30 (2014) 337–355.
[10] A.A. Yaroshevsky, Abundances of chemical elements in the earth's crust, Geochem. Int. 44 (2006) 48–55.
[11] S. LeBlanc, Thermoelectric generators: linking material properties and systems engineering for waste heat recovery applications, Sustain. Mater. Technol. 1–2 (2014) 26–35.
[12] J. He, Y. Liu, R. Funahashi, Oxide thermoelectrics: the challenges, progress, and outlook, J. Mater. Res. 26 (2011) 1762–1772.
[13] I. Terasaki, Y. Sasago, K. Uchinokura, Large thermoelectric power in $NaCo_2O_4$ single crystals, Phys. Rev. B 56 (1997) 12685–12687.
[14] X. Wang, H. Wang, W. Su, T. Chen, C. Tan, M.A. Madre, A. Sotelo, C. Wang, U-type unileg thermoelectric module: a novel structure for high-temperature application with long lifespan, Energy 238 (2022) 121771.
[15] H. Leligny, D. Grebille, O. Perez, A.C. Masset, M. Hervieu, B. Raveau, A five-dimensional structural investigation of the misfit layer compound $[Bi_{0.87}SrO_2]_2[CoO_2]_{1.82}$, Acta Crystallogr. B 56 (Part 2) (2000) 173–182.
[16] A.C. Masset, C. Michel, A. Maignan, M. Hervieu, O. Toulemonde, F. Studer, B. Raveau, J. Hejtmanek, Misfit-layered cobaltite with an anisotropic giant magnetoresistance: $Ca_3Co_4O_9$, Phys. Rev. B 62 (2000) 166–175.
[17] T. Chen, J. Wang, X. Wang, H. Wang, W. Su, J. Zhai, F. Mehmood, M. Khan, C. Wang, Cross-scale porous structure design leads to optimized thermoelectric performance and high output power for $CaMnO_3$ ceramics and their uni-leg modules, Appl. Mater. Today 29 (2022) 101557.
[18] A. Maignan, D. Pelloquin, S. Hébert, Y. Klein, M. Hervieu, Thermoelectric power in misfit cobaltites ceramics: optimization by chemical substitutions, Bol. Soc. Esp. Ceram. V. 45 (2006) 122–125.
[19] J. Yao, T. Chen, H. Wang, M. Khan, C. Tan, Y. Sun, W. Su, H. Wang, C. Wang, Stable cubic crystal structures and optimized thermoelectric performance of $SrTiO_3$-based ceramics driven by entropy engineering, J. Mater. Chem. A 10 (2022) 24561–24572.
[20] H. Wang, X. Sun, X. Yan, D. Huo, X. Li, J.-G. Li, X. Ding, Fabrication and thermoelectric properties of highly textured $Ca_9Co_{12}O_{28}$ ceramic, J. Alloys Compd. 582 (2014) 294–298.
[21] J.G. Noudem, D. Kenfaui, D. Chateigner, M. Gomina, Granular and lamellar thermoelectric oxides consolidated by spark plasma sintering, J. Electron. Mater. 40 (2011) 1100–1106.
[22] J.C. Diez, Sh. Rasekh, G. Constantinescu, M.A. Madre, M.A. Torres, A. Sotelo, Effect of annealing on the thermoelectric properties of directionally grown $Bi_2Sr_2Co_{1.8}O_x$ ceramics, Ceram. Int. 38 (2012) 5419–5424.
[23] A. Maignan, S. Hébert, M. Hervieu, C. Michel, D. Pelloquin, D. Khomskii, Magnetoresistance and magnetothermopower properties of Bi/Ca/Co/O and Bi (Pb)/Ca/Co/O misfit layer cobaltites, J. Phys. Condens. Matter 15 (2003) 2711–2723.
[24] N. Kikugawa, D.A. Sokolov, T. Nagasawa, A.P. Mackenzie, Single-crystal growth of Sr_2RuO_4 by the floating-zone method using an infrared image furnace with improved halogen lamps, Crystals 11 (2021) 392.
[25] R.S. Feigelson, D. Gazit, D.K. Fork, T.H. Geballe, Superconducting Bi-Ca-Sr-Cu-O fibers grown by the laser-heated pedestal growth method, Science 240 (1988) 1642–1645.

[26] A. Revcolevschi, J. Jegoudez, Growth of large high-Tc single crystals by the floating zone method: a review, Prog. Mater. Sci. 42 (1997) 321–339.

[27] F.M. Costa, N.M. Ferreira, Sh. Rasekh, A.J.S. Fernandes, M.A. Torres, M.A. Madre, J.C. Diez, A. Sotelo, Very large superconducting currents induced by growth tailoring, Cryst. Growth Des. 15 (2015) 2094–2101.

[28] J.C. Diez, Sh. Rasekh, G. Constantinescu, M.A. Madre, M.A. Torres, A. Sotelo, Effect of annealing on the thermoelectric properties of directionally grown $Bi_2Sr_2Co_{1.8}O_x$ ceramics, Ceram. Int. 38 (2012) 5419–5424.

[29] E. Combe, R. Funahashi, T. Barbier, F. Azough, R. Freer, Decreased thermal conductivity in $Bi_2Sr_2Co_2O_x$ bulk materials prepared by partial melting, J. Mater. Res. 31 (2016) 1296–1305.

[30] Sh. Rasekh, F.M. Costa, N.M. Ferreira, M.A. Torres, M.A. Madre, J.C. Diez, A. Sotelo, Use of laser technology to produce high thermoelectric performances in $Bi_2Sr_2Co_{1.8}O_x$, Mater, Design 75 (2015) 143–148.

[31] O. Jankovsky, D. Sedmidubsky, Phase equilibria modelling in Bi–Sr–Co–O system-Towards crystal growth and melt-assisted material processing, J. Eur. Ceram. Soc. 38 (2018) 131–135.

[32] M. Kato, Y. Goto, K. Umehara, K. Hirota, K. Yoshimura, Synthesis and physical properties of Bi–Sr–Co-oxides with 2D-triangular Co layers intercalated by iodine, Physica B 378–380 (2006) 1062–1063.

[33] T. Itoh, I. Terasaki, Thermoelectric properties of $Bi_{2.3-x}Pb_xSr_{2.6}Co_2O_y$ single crystals, Jpn. J. Appl. Phys. 39 (2000) 6658–6660.

[34] D. Mercurio, J.C. Champarnaud-Mesjard, B. Frit, P. Conflant, J.C. Boivin, T. Vogt, Thermal evolution of the crystal structure of the rhombohedral $Bi_{0.75}Sr_{0.25}O_{1.375}$ phase: a single crystal neutron diffraction study, J. Solid State Chem. 112 (1994) 1–8.

[35] G.F. de la Fuente, J.C. Diez, L.A. Angurel, J.I. Pena, A. Sotelo, R. Navarro, Wavelength dependance in laser floating zone processing. A case study with Bi-Sr-Ca-Cu-O superconductors, Adv. Mater. 7 (1995) 853–856.

[36] F.M. Costa, N.M. Ferreira, Sh. Rasekh, A.J.S. Fernandes, M.A. Torres, M.A. Madre, J.C. Diez, A. Sotelo, Very large superconducting currents induced by growth tailoring, Cryst. Growth Des. 15 (2015) 2094–2101.

[37] R. Funahashi, I. Matsubara, S. Sodeoka, Thermoelectric properties of $Bi_2Sr_2Co_2O_x$ polycrystalline materials, Appl. Phys. Lett. 76 (2000) 2385–2387.

[38] S.-T. Dong, B.-B. Zhang, L.-Y. Zhang, Y.B. Chen, S.-H. Yao, J. Zhou, S.-T. Zhang, Z.-B. Gu, Y.-F. Chen, Metal-semiconductor-transition observed in $Bi_2Ca(Sr,Ba)_2Co_2O_{8+\delta}$ single crystals, Appl. Phys. Lett. 105 (2014) 042105.

[39] W. Shin, N. Murayama, Thermoelectric properties of (Bi,Pb)–Sr–Co–O oxide, J. Mater. Res. 15 (2000) 382–386.

[40] H. Itahara, C. Xia, J. Sugiyama, T. Tani, Fabrication of textured thermoelectric layered cobaltites with various rock salt-type layers by using β-Co(OH)$_2$ platelets as reactive templates, J. Mater. Chem. 14 (2004) 61–66.

[41] P. Wang, M. Fan, Y. Zhang, X.-J. Li, H. Song, Effects of SiC doping on the thermoelectric properties of $Bi_{1.9}Ba_{0.1}Sr_2Co_2O_y$ Ceramics, Ceram. Int. 47 (2021) 25045–25050.

[42] B. Ozkurt, M.A. Madre, A. Sotelo, M.A. Torres, Enhanced thermoelectric properties in $Bi_2Sr_{2-x}Ba_xCo_2O_y$ ceramics by Ba doping, Physica B 643 (2022) 414138.

[43] H.Y. Hong, S.Y. Gwon, D. Kim, K. Park, Influence of sintering temperature and Li^+/Mg^{2+} doping on the thermoelectric properties of $Bi_{2-2x}Li_xMg_xSr_2Co_2O_y$, Adv. Appl. Ceram. 121 (2022) 124–131.

[44] H.Y. Hong, S.Y. Gwon, S.O. Won, K. Park, Enhanced thermoelectric properties of Ce-doped $Bi_2Sr_2Co_2O_y$ misfit-layer oxides, J. Mater. Res. Technol. 19 (2022) 1873–1883.

[45] N. Sun, S.T. Dong, B.B. Zhang, Y.B. Chen, J. Zhou, S.T. Zhang, Z.B. Gu, S.H. Yao, Y. F. Chen, Intrinsically modified thermoelectric performance of alkaline-earth isovalently substituted $[Bi_2AE_2O_4][CoO_2]_y$ single crystals, J. Appl. Phys. 114 (2013) 043705.

[46] M.A. Madre, Sh. Rasekh, J.C. Diez, A. Sotelo, New solution method to produce high performance thermoelectric ceramics: a case study of Bi-Sr-Co-O, Mater. Lett. 64 (2010) 2566–2568.

[47] M.A. Madre, F.M. Costa, N.M. Ferreira, S.I.R. Costa, Sh. Rasekh, M.A. Torres, J. C. Diez, V.S. Amaral, J.S. Amaral, A. Sotelo, High thermoelectric performance in $Bi_{2-x}Pb_xBa_2Co_2O_x$ promoted by directional growth and annealing, J. Eur. Ceram. Soc. 36 (2016) 67–74.

[48] R. Funahashi, M. Shikano, $Bi_2Sr_2Co_2O_y$ whiskers with high thermoelectric figure of merit, Appl. Phys. Lett. 81 (2002) 1459–1461.

[49] M. Fan, Y. Zhang, X.-J. Li, H. Song, High thermoelectric performance in nano-SiC dispersed $Bi_{1.6}Pb_{0.4}Sr_2Co_2O_y$ compounds, J. Alloys Compd. 825 (2020) 154065.